Surface Deformation and Seismicity Induced by Poroelastic Stress at the Raft River Geothermal Field, Idaho, USA

Bing Qiuyi Li[1], Mostafa Khoshmanesh[1], and Jean-Philippe Avouac[1]

[1]California Institute of Technology

November 24, 2022

Abstract

We investigate the relative importance of injection and production on the spatial-temporal distribution of induced seismicity at the Raft River geothermal field. We use time-series of inSAR measurements to document surface deformation and calibrate a hydro-mechanical model to estimate effective stress changes imparted by injection and production. Seismicity, located predominantly in the basement, is induced primarily by poroelastic stresses from cold water reinjection into a shallower reservoir. The poroelastic effect of production from a deeper reservoir is minimal and inconsistent with observed seismicity, as is pore-pressure-diffusion in the basement and along reactivated faults. We estimate an initial strength excess of 20kPa in the basement and sedimentary cover, but the seismicity rate in the sedimentary cover is 4 times lower, reflecting lower density of seed-points for earthquake nucleation. Our modeling workflow could be used to assess the impact of fluid extraction or injection on seismicity and help design or guide operations.

1

Surface Deformation and Seismicity

Induced by Poroelastic Stress at the Raft

River Geothermal Field, Idaho, USA

Bing Q. Li[1†], Mostafa Khoshmanesh[2], Jean-Philippe Avouac[1]

[1] Division of Geological and Planetary Sciences, California Institute of Technology, CA, USA

[2] Department of Mechanical and Civil Engineering, California Institute of Technology, CA, USA

† Now at Department of Civil and Environmental Engineering, Western University, ON, Canada

Corresponding author: Bing Q. Li (bingqli@caltech.edu)

Key Points

- A hydro-mechanical model of effective stress changes from injection and production is calibrated using surface deformation from InSAR

- Seismicity, located predominantly in the basement, is primarily induced by poroelastic stress changes from cold water re-injection

- Similar stress changes trigger 4 time more earthquakes per unit volume in the basement than in the sedimentary cover.

17 Abstract

18 We investigate the relative importance of injection and production on the spatial-temporal distribution

19 of induced seismicity at the Raft River geothermal field. We use time-series of InSAR measurements to

20 document surface deformation and calibrate a hydro-mechanical model to estimate effective stress

21 changes imparted by injection and production. Seismicity, located predominantly in the basement, is

22 induced primarily by poroelastic stresses from cold water reinjection into a shallower reservoir. The

23 poroelastic effect of production from a deeper reservoir is minimal and inconsistent with observed

24 seismicity, as is pore-pressure-diffusion in the basement and along reactivated faults. We estimate an

25 initial strength excess of ~20kPa in the basement and sedimentary cover, but the seismicity rate in the

26 sedimentary cover is 4 times lower, reflecting lower density of seed-points for earthquake nucleation.

27 Our modeling workflow could be used to assess the impact of fluid extraction or injection on seismicity

28 and help design or guide operations.

29 Plain Language Summary

30 It is important to understand the mechanisms behind human-induced earthquakes, whether they are

31 beneficial in the context of generating fractures for effective geothermal energy systems, or hazardous

32 in the case of large earthquakes that may cause structural damage. Here, we present a case study of the

33 Raft Rive geothermal field, which has operated since 2007 and generated earthquakes since 2010. Our

34 objective is to understand how hot water, which is extracted from a deep sedimentary layer, and cold

35 water, which is injected into a shallower layer, contribute to the observed seismicity, which have

36 primarily occurred underneath the extraction layer. We construct a model to determine how the

37 injection and extraction affect underground fluid pressures, and how these pressures impart stresses

38 throughout the subsurface. This model is calibrated using InSAR, a satellite-based technique which

39   provides precise measurements the Earth's surface deformation in time. The results show that the

40   shallow cold water injection is main culprit behind the deep earthquakes, because of the stresses

41   imparted by the fluid pressure increase, whereas the effects of the deep extraction is negligible. Our

42   modeling workflow could be used to assess the impact of fluid extraction or injection on seismicity and

43   help guide operations.

44   1 Introduction

45   Injection and extraction of fluids from the subsurface can induce earthquakes (*e.g.*, Ellsworth, 2013).

46   Induced seismicity can be intentional and beneficial. This is the case in the context of Enhanced

47   Geothermal Systems where hydrofractures and shear-fractures are used to enhance permeability

48   (Elsworth et al., 2016). In the context of CO2 storage, fracturing of the underburden, the rock volume

49   beneath the target reservoir, could enhance the storage capacity. Most commonly though, seismicity is

50   viewed as a source of hazard that can compromise the safe operation of a geothermal field or of a CO2

51   storage site (Zoback and Gorelick, 2012; Elsworth et al., 2016). In any case, there is much need for a

52   better understanding of how such operations could induce earthquakes.

53   It is well established that the Coulomb Failure Stress change, ΔCFS, can be used to assess the risk of

54   induced seismicity due to a stress change at a particular location (King et al., 1994; Stein, 1999). An

55   increase of ΔCFS can in principle result from an increase of shear stress, an increase of pore pressure, or

56   decrease of normal stress. In the case of fluid injection or extraction, ΔCFS at a given location might be

57   due to pore pressure diffusion or due to thermo- or poroelastic stress changes (*e.g.*, Segall et al., 1994;

58   Segall and Fitzgerald, 1998; Goebel and Brodsky, 2018). The effect of pressure diffusion might, in

59   principle, be identified from the migration pattern of seismicity (*e.g.*, Shapiro et al.., 1997). By contrast,

60   poroelastic stresses due to a well operation are imparted almost instantaneously and should result in a

61   spatially stationary pattern which can reach large distances shortly after injection (Goebel et al, 2017;

62   Zhai and Shirzaei, 2019). In reality, disentangling the relative role of these mechanisms is often

63   challenging. One reason is that the temporal evolution of seismicity also depends on the earthquake

64   nucleation process, so that it does not reflect instantaneous stress changes (*e.g.*, Dieterich, 1994; Zhai

65   and Shirzaei, 2019; Alghannam and Juanes, 2020). Another reason is that field operations often involve a

66   complex set of injecting and extracting wells (*e.g.*, Hornbach et al., 2015); assigning seismicity to

67   particular sources of stresses is therefore often ambiguous in such a context.

68   Here we study the case-example of seismicity induced at the Raft River geothermal field, which is

69   particularly appropriate to gain insight into induced earthquake triggering mechanisms (Figure 1). The

70   number of wells is relatively small and the geological setting is simple and well documented (*e.g.*,

71   Bradford et al., 2013; Nash and Moore, 2012). In addition, a prominent geodetic signal has been

72   previously observed using Synthetic Aperture Radar Interferometry, InSAR (Liu et al., 2018; Ali et al,

73   2018). Such measurements can indeed provide important constraints on the spatio-temporal evolution

74   of the pressure field and fluid flow in the sub-surface reservoirs (Ali et al., 2018, Hoffmann et al., 2001;

75   Chaussard et al., 2014). Finally, and most importantly for the purpose of this study, local seismic

76   monitoring has revealed seismicity clearly correlated with the geothermal field (Figure 1a). One

77   interesting specific feature of the raft River geothermal field is that hot water is produced from a ~100m

78   thick reservoir at a depth of ~1500m below surface, and the cold water is reinjected in a distinct ~300m

79   thick shallower reservoir at 500m depth below surface.

80   Given that the production reservoir directly overlies the seismogenic basement, it is unlikely that pore

81   pressure diffusion into the basement is responsible for the observed seismicity. If the zone of seismicity

82   were hydraulically connected to the reservoir, fluid extraction should have decreased the pore pressure,

83   leading to fault strengthening. As a result, the thermo- and poroelastic contributions from production

84   and injection are perhaps the primary mechanisms behind the induced seismicity. Hereafter, we first

85   give an overview of the setting of the Raft River geothermal field. We next present the methods used to

86   model surface deformation and effective stress changes in the sub-surface. In the results section, we

87   investigate the relative importance of injection and production on the spatial and temporal distribution

88   of induced seismicity.

89   2 Setting of the Raft River Geothermal field

90   The Raft River geothermal site was identified in the 1950s, first developed as a DOE demonstration site

91   in the 1970s, and significant production started by the end of 2007. The geology and geomechanical

92   properties of the subsurface is relatively well documented in publicly available documents thanks to

93   investigations conducted by the USGS and recent studies, and in relation to the recent EGS

94   demonstration (Nash and Moore, 2012; Bradford et al., 2014, Bradford et al., 2015; Yuan et al, 2020).

95   The Miocene to Pliocene sedimentary cover is about 1.5-2 km thick and consists of sub-horizontal

96   interbedded volcanoclastics, volcanics, sandstones, and siltstones. It overlies a proterozoic metamorphic

97   basement consisting of quartzite, schist and quartz monzonite. The area is part of the Basin-and-range

98   zone of ~East-West active extension. Historical seismicity rates were however very low prior to

99   production, with normal-faulting focal mechanisms broadly consistent with E-W extension (Zandt et al.,

100   1982). Well logs show steeply dipping fractures trending approximately N-S (Bradford et al., 2013; Nash

101   and Moore, 2012).

102   Hot water is extracted at a depth of ~1500m below surface from a ~100m thick quartzite layer through

103   four wells (Figure 1b). One well, RRG-9 (Figure 1), was found to be poorly connected to the geothermal

104   reservoir and selected for an Enhanced Geothermal System (EGS) stimulation. To avoid thermal

105   drawdown, the cold water is injected through three wells into a shallower reservoir at a depth of

106   approximately 500m below surface. This reservoir consists of Late Miocene tuff, about 300m thick.

107   In this study we used the baseline mechanical, hydrological, and poroelastic parameters of the reservoir

108   rocks determined in previous hydro-thermal-mechanical studies (Liu et al., 2018; Yuan et al., 2020;

109   Bradford et al., 2014) (Table 1). The reservoir permeability and compressibility were then calibrated to

110   the geodetic data (Supplement 1) to better constrain the pore pressure diffusion and poroelastic stress

111   change models respectively.

112   Significant production started only by the end of 2007 and ramped up gradually until 2010. The site was

113   selected for an Enhanced Geothermal System (EGS) demonstration by DOE. The EGS demonstration was

114   conducted at well RRG-9 over three phases between February 2012 and April 2014 with the goal of

115   using hydraulic stimulation to improve the injectivity of the surrounding reservoir. Each phase consisted

116   of cold fluid injection followed by a shut-in period to assess the pressure falloff characteristics. The well

117   has since been used for continuous commercial use.

118   The Lawrence Berkeley National Laboratory deployed a local seismic network consisting of 10 stations

119   which started operating in early 2010 (Supplementary Figure S2). Their seismicity catalog shows

120   seismicity clearly clustered in the vicinity of the geothermal field, and correlated with the surface

121   deformation pattern measured from InSAR (Figure 1a). Seismicity is located primarily in the

122   metamorphic basement immediately underlying the production reservoir. It started in late 2010, lagging

123   the onset of large-scale production by about 2 years and pre-dating the EGS stimulation. We note that

124   the magnitude of completeness appears to decrease from $M_c \sim 0.5$ prior to the EGS stimulation, to $M_c \sim$

125   0 during and after the EGS stimulation. The seismicity cluster along a steeply dipping zone trending

126   ~N60^{o}E which coincides with the Narrows Fault zone, a basement structure which had been inferred

127   from geophysical and hydrological studies (Bradford et al., 2013; Dolenc et al., 1981).

128 3 Geomechanical Modelling

129 In our formulation, we account for the effects of pore pressure diffusion and its resultant poroelastic

130 stress changes. We do not consider thermal effects given that the thermal contrasts are generally most

131 important for injection of cold water, and the injection reservoir is very shallow (~500m depth) so that

132 the poroelastic effects would dominate over the thermal effects as observed at the Salton Sea

133 Geothermal Field in Southern California (Barbour et al., 2016). In the production reservoir, fluid

134 extraction should only cause minor thermal effects as heat is advected horizontally, and so the

135 horizontal temperature gradients should be small. This is corroborated by Liu et al's study (2018), where

136 their coupled hydro-thermal-mechanical model of the Raft River geothermal field predicts that the

137 poroelastic effects of fluid extraction and injection would dominate for the first 10 years, and the long-

138 term effects of cooling in the injection reservoir would only emerge after 20 years of production.

139 In our workflow, we calculate the pressure change in the reservoir resulting from fluid injection and

140 extraction, the surface displacements for comparison with the InSAR measurement, and the stresses in

141 the basement and overlying sedimentary cover for comparison with the observed seismicity. We choose

142 to employ analytical solutions here as they minimize the number of model parameters while providing

143 an excellent fit to the geodetically measured surface deformation data. In addition, they are

144 computationally inexpensive, which can enable, in principle, scaling to larger systems involving

145 thousands of wells.

146 Given that the geology of the Raft River site can be generally considered as a vertically layered system

147 (Liu et al., 2018), we employ a 2D axisymmetric model for pore pressure diffusion, where the pore

148 pressure changes corresponding to production and injection can be considered separately in what we

149 assume are unconnected reservoirs. In this formulation, considering a single well, the pore pressures at

150 a given time, t, and a given location, $x = (x_1, x_2)$, from the well is,

151

$$P(x,t)=\frac{1}{H\rho_0 4\pi\kappa}\int_0^t q(t')\frac{\exp\left[\frac{-r'^2}{4c(t-t')}\right]}{t-t'}dt' \tag{1}$$

152   where q(t') is the mass flow rate, c is the diffusivity, ρ_0 is the reference density, H is the thickness of the

153   layer, $\kappa = k/\eta$, k is the permeability, and η is the fluid viscosity. This solution is taken from Rudnicki

154   (1986), which we modified to allow anisotropy of the pore pressure diffusion, given that the surface

155   displacement (Figure 1a) suggests higher permeability in the ~N-S direction. The anisotropy is

156   implemented by transforming the radius r into an elliptical anisotropic radius r' defined as

$$r'=\frac{\xi\sqrt{x_1^2+x_2^2}}{\sqrt{\xi^2\sin^2(\theta-\varphi)+\cos^2(\theta-\varphi)}} \tag{2}$$

157   where ξ is the anisotropy factor, φ is the anisotropy angle of the direction of low permeability, and

158   $\theta=atan\left(\frac{x_2}{x_1}\right)$. The pressure changes are calculated independently for each injection and production

159   well, and superposed for all wells within the same reservoir.

160   Given the pore pressure distribution in the production and injection reservoirs, the induced poroelastic

161   stress and displacement fields can be approximated by gridding the pore pressure solution following

162   Kuvshinov (2008). The solutions for the entire stress tensor and displacement vector can be found in the

163   supplementary materials.

164   We evaluate the displacement at the surface (Supplement 1) and calibrate the model parameters using

165   the geodetic measurements. We also evaluate the stress changes in the basement and the sedimentary

166   cover in order to compare with seismicity. The stress changes are rotated to obtain normal and shear

167   components on a strike-slip fault oriented at N60°E with 76° dip corresponding to the Narrows fault

168   zone (Nash and Moore, 2012), and consistent with the orientation of the seismicity cluster. We calculate

169   the Coulomb failure stress (CFS) change

$$\Delta CFS = \Delta\tau + \mu\left(\Delta\sigma_n + \Delta P\right),\qquad(6)$$

170   where $\Delta\tau$ is the change in shear stress on the fault, $\Delta\sigma_n$ is the change in normal stress, ΔP is the change

171   in pore pressure, and $\mu=0.6$ is the friction coefficient.

172 4 Results

173   We use a volume rate of 0.1 m^3/s for injection wells, and 0.075 m^3/s for production wells following Liu et

174   al. (2018), with a ramp-up time of two years. We also include the effect of the EGS injection at well RRG-

175   9 ST1 (Figure 1) using the data reported in the thesis by Bradford (2016), discretized into monthly rates.

176   To calibrate the model, we generate a range of model realizations for the surface displacement, and

177   select the model parameters that minimize the misfit between the modelled and geodetically measured

178   surface displacement. We vary the injection and production reservoir compressibility in the

179   poroelasticity formulation continuously, and permeability in the pore pressure formulation discretely.

180   We simulate 1 million instances of these parameters, and compare the 1D histogram of the modelled

181   displacement at any given time sample with the corresponding measured displacement using the

182   Wasserstein distance (Ramdas et al., 2017). We choose the Wasserstein distance as a goodness-of-fit

183   criterion for the 1D histogram as it allows us to consider the distribution of positive and negative surface

184   displacements while being insensitive to the exact spatial location of the bulb of uplift. The best-fit

185   parameters for permeability and compressibility are given in Table 1. The uncertainty in the discretely

186   sampled permeability is given as the width of the sampling bin, given that the best-fit value was

187   preferred in all simulated instances. We determine the uncertainty for the continuously sampled

188   compressibility parameter using a bootstrap method where we consider 100,000 subsamples of size

189   10,000 and select the best fitting model from each subsample. We then consider the 95% confidence

190   interval as the 2.5[th] and 97.5[th] percentile values from the population of best-fit compressibility values

191   (Supplementary Figure S1), and how the uncertainty affects the CFS change.

192   Figure 1a shows the spatial distribution of vertical displacement rate averaged from 2007 to 2011, which

193   shows a clear signal of uplift around the injection wells. These wells are injecting at 500m below the

194   surface, and thus have a stronger signature across a smaller footprint compared to the production which

195   occurs at a deeper depth of ~1.5 km below the surface. The elliptical bulb of uplift is well captured by

196   our model (Figure 1b) estimated over the same time period of 2007 to 2011, which similarly shows

197   highly localized uplift that is elongated in the NW-SE direction and generally captures the transition

198   distance from uplift to subsidence. The isotropic model (Supplementary Figure S3) predicts an E-W

199   elongated uplift pattern due to the distribution of wells that fails to match this feature. The elliptical

200   shape of the zone of uplift is reproduced well by our pore pressure diffusion model thanks to the

201   inclusion of anisotropy. The best-fitting permeability for the injection reservoir is 5.9 ± 1.5 x 10^{-13} m^2 in

202   the direction of slow diffusion, which is trending N70°E, and 8.3 ± 2 x 10^{-13} m^2 in the direction of fast

203   diffusion, which is trending N20°W. The N70°E permeability is within error from the value of 4.7 x 10^{-13}

204   m^2 used by Liu et al. (2018), while the N20°W permeability indicates faster diffusion than predicted in

205   their study. The permeability anisotropy is possibly due to the pre-existing fractures which are oriented

206   ~N-S (Nash and Moore, 2012; Liu et al., 2018). The N20°E direction of fast diffusion and the anisotropy

207   factor of 1.4 is also consistent with the analysis of Yuan et al., (2020), who found the permeability to be

208   larger by a factor 1.2 to 2 along the NNE-SSW direction compared to the orthogonal direction.

209   Our model also reproduces the temporal behavior shown in Figure 1d, with an initial rapid uplift at

210   location "A" before 2010, which then transitions to a steady-state with no further uplift. The seismicity is

211   located within the general vicinity of the injection and production wells as shown in Figure 1, and begin

212   in the basement in mid-2010 then continue in swarms of activity.

213   Figure 2a and 2b show the reservoir pressures resulting from injection and production respectively. As

214   expected, these sources generate increased and decreased pore pressures in their respective reservoirs.

215   Note that the effect of the stimulation of well RRG-9 is not visible due to the very small injection volume

216   (Figure 3b). The resultant poroelastic stress changes in the basement, shown for April 2014 in Figure 2c

217   and 2d for injection and production respectively, indicate that the poroelastic contributions to Coulomb

218   failure stress (CFS) changes affect fault stability in the same manner as the pore pressures, i.e. injection

219   causes increases in CFS due to both pore pressure and poroelastic effects, and vice versa for the

220   production. As a result, the total CFS change in the basement (Figure 3a) suggests that injection is

221   primarily responsible for the observed induced seismicity, which occur almost exclusively in the regions

222   of positive CFS change. To explore the sensitivity to the assumed fault plane orientation, we test

223   different receiver fault orientations and find that the zone of increased CFS change around the injection

224   and production wells is largely unchanged. See Supplementary Figure S4 for the case of left-lateral and

225   normal N-S faults parallel to regional documented faults (Nash and Moore, 2012).

226   The time evolution of CFS at the location of maximum uplift (point A) and the edge of the seismicity

227   cloud (point B) suggests that the eastern edge of the seismicity is dominated entirely by stresses from

228   the injection, while stresses on the western edge of the seismicity are inhibited significantly by the

229   production (Figure 3c). Note that the pressure evolution at point B, located near well RRG-9, shows a

230   very short-lived pressure increase. This figure also shows that although the simulation assumes a simple

231   ramp to constant flow rate from 2008 to 2010, the zone of Coulomb stress increase due to poroelastic

232   loading of the basement keeps increasing until the end of the simulation as the zone of high pore

233   pressure in the shallow reservoir expands away from the injection wells. This can explain the sustained

234   seismic activity. Additionally, the CFS change at "A" as shown in Figure 3c indicates there may be a

235   critical Coulomb stress increase of approximately 50kPa required to trigger the seismicity. That would

236   represent the initial strength excess, i.e. the initial distance from the failure criterion, within the

237 Narrows fault zone. To further investigate this, we calculate the CFS change at the specific origin time

238 and hypocentral location of the observed earthquakes (Figure 4a). In this calculation we assume the

239 same hypocentral depth of 500m for events in the basement, and -500m for events in the overlying

240 sedimentary cover. We can see that nucleation stresses range from 0 to 70kPa for events in the

241 basement and the overlying sedimentary cover, and the histograms shown in Figure 4b and 4c show a

242 possibly bimodal distribution of nucleation stress for the basement with a main mode at 19kPa. It is

243 interesting that the two histograms are actually quite similar despite the fact that very few earthquakes

244 occurred in the sedimentary cover. According to our analysis a given volume of basement rocks

245 submitted to a given ΔCFS produces 4 times more earthquakes than the same volume of sedimentary

246 rocks submitted to the same ΔCFS. This is because the earthquake productivity, representing the density

247 of possible nucleation points of earthquake with magnitude larger than the detection threshold, must be

248 4 times larger in the basement than in the sedimentary cover (Figure 4d).

249 Given the magnitude of the pore pressure changes in the production reservoir, which are about 100

250 times larger than the magnitude of the poroelastic stress changes, we believe it is justified to consider

251 the production reservoir to be uncoupled from the basement, otherwise we would not expect any

252 seismicity whatsoever since the pore pressure reduction from extraction would completely dominate

253 the state of stress in the basement. We account for the hydraulic stimulation at RRG-9-ST1 as an

254 additional injection well located in the production reservoir, although we note that its corresponding

255 pore pressure contributions are small relative to the standard production wells given the low injection

256 volumes (Figure 3b). This can be seen in the stress changes at point "B" (Figure 3c), which is located

257 close to well RRG-9 but only experiences small stress changes on the order of ~1kPa as a result of the

258 stimulation at the well. Considering the spatial distribution of seismicity prior to the first stimulation

259 phase, we see that the majority of the central seismicity cloud is already activated before March 2012

260 even with the lower magnitude of completeness (Supplementary Figure S2), and so the hydraulic

261 stimulations likely did not significantly affect the hydraulic connection between the basement and the

262 production reservoir. This is supported by the observation that we do not generally see spatial diffusion

263 of earthquake events away from well RRG-9 after the three stimulation events (Supplementary Figure

264 S2c).

265 5 Discussion and Conclusions

266 Together with previous studies which have adopted a similar strategy (Juanes et al., 2016; Shirzaei et al.,

267 2016), our study demonstrates the value of combining observation of surface deformation and simple

268 fluid flow and geomechanical modeling to analyze induced seismicity due to injection and extraction of

269 fluids from the subsurface. We acknowledge that our evaluation of uncertainties incorporates only the

270 sensitivity of our analytical solution, and does not account for potential sources of correlated error in

271 the InSAR measurements (*e.g.* tropospheric corrections, ionospheric effects) or epistemic uncertainties

272 relating to our assumption of homogeneous reservoir properties in a homogeneous elastic half-space.

273 Nevertheless, we believe that our main findings, at least qualitatively, are not dependent on these

274 uncertainties, given the similarity of our modelled and measured surface displacements with previous

275 works (Liu et al., 2018; Ali et al., 2018), as well as our ability to resolve the permeability anisotropy

276 suggested by Yuan et al. (2020).

277 The spatial distribution of ΔCFS contributions (Figs 2c, 2d) in the basement strongly suggest that

278 poroelastic stress changes from shallow injection is responsible for the timing and location of observed

279 induced seismicity. The pore pressures from injection are not connected to the basement and the

280 poroelastic stress changes resulting from fluid extraction are smaller in magnitude compared to the

281 injection. Figure 3a, which shows the net ΔCFS in the basement, indicates that all earthquake events

282 occur in the region of positive slip potential, which suggests that while the magnitude of the

283 contribution from production is small, it nevertheless has an inhibiting effect on fault slip potential, for

284   example in the region to the north of well RRG-9 ST1. In terms of the distribution of ΔCFS at the time

285   and location of earthquake nucleations (Figure 4), we also find that the basement has an initial strength

286   excess of approximately 15 – 20kPa, and an excess of 20 – 25kPa in the overlying sedimentary cover

287   which is required to activate the fault, similar to the observations at Groningen by Smith (2019).

288   In terms of the timing of seismicity in relation to the DOE hydraulic fracturing project at well RRG-9 ST1,

289   our results show that the seismicity begins in late 2010 whereas the first phase at well RRG-9 ST1 begins

290   in early 2012. This, in conjunction with the minimal CFS changes at "B" (located close to well RRG-9 ST1)

291   in Figure 3c, show that while the project did indeed trigger some induced events (Bradford, 2016), the

292   timing and location nevertheless correspond to the larger-scale spatial distribution of CFS change shown

293   in Figure 3a.

294   Overall, our results show that the observed spatial and temporal distribution of surface deformation and

295   induced seismicity at the Raft River geothermal site may be reasonably explained by simple analytical

296   solutions for axisymmetric pore pressure diffusion and its resultant poroelastic stress changes. Our

297   model uses only a simplified 1D geological model as well as injection and production rates as inputs,

298   where geomechanical parameters are constrained by fitting the modelled surface displacement to the

299   true surface displacement as observed by InSAR measurements. This simple framework is scalable and

300   easily calibrated given the small number of parameters, and can be readily applied to investigate large

301   multi-well systems involving combined injection and production such as Oklahoma and Texas

302   (Langenbruch and Zoback, 2016; Zhai et al., 2018; Walter et al., 2018), where existing studies are

303   primarily focused on the effects of fluid injection. Our framework may be used to inform geothermal

304   and carbon storage strategies, where the seismicity in the basement and elsewhere could in principle be

305   controlled by regulating the injection rates (Kwiatek et al., 2019; Birkholzer et al., 2012; Cihan et al.,

306   2015). We conjecture that, using the modeling workflow presented in this study, the location and time-

307   evolution of seismicity induced by fluid extraction could in principle be controlled by adjusting well flow

308   rates.

Acknowledgements

References

Alghannam, M. & Juanes, R., 2020. Understanding rate effects in injection-induced earthquakes, *Nature Communications*, 11.

Ali, S.T., Reinisch, E.C., Moore, J., Plummer, M., Warren, I., Davatzes, N.C., Feigl, K.L. (2018) Geodetic measurements and numerical models of transient deformation at Raft River geothermal field, Idaho, USA. *Geothermics*, 74, 106-111, doi: 10.1016/j.geothermics.2018.02.007

Barbour, A.J., Evans, E.L., Hickman, S.H., Eneva, M. (2016) Subsidence rates at the southern Salton Sea consistent with reservoir depletion. *Journal of Geophysical Research: Solid Earth*, 121, 5308–5327, doi:10.1002/2016JB012903

Birkholzer, J.T., Cihan, A. & Zhou, Q., 2012. Impact-driven pressure management via targeted brine extraction-Conceptual studies of CO_2 storage in saline formations, *International Journal of Greenhouse Gas Control*, 7, 168-180.

Bourne, S.J., Oates, S.J., van Elk, J., Doornhof, D. (2014) A seismological model for earthquakes induced by fluid extraction from a subsurface reservoir. *Journal of Geophysical Research*: *Solid Earth*, 119(12), 8991-9015, doi: 10.1002/2014JB011663

Bourne, S.J. & Oates, S.J., 2017. Extreme Threshold Failures Within a Heterogeneous Elastic Thin Sheet and the Spatial-Temporal Development of Induced Seismicity Within the Groningen Gas Field, *Journal of Geophysical Research-Solid Earth*, 122, 10299-10320.

Bradford, J.T. (2016) The Application of Hydraulic and Thermal Stimulation Techniques to Create Enhanced Geothermal Systems (Doctoral Dissertation)

Bradford, J., McLennan, J., Moore, J., Glasby, D., Waters, D., Kruwell, R., Bailey, A., Rickard, W., Bloomfield, K., King, D. (2013) Recent developments at the Raft River geothermal field. In: *Proceedings of the 38th workshop on geothermal reservoir engineering*, Stanford, CA 2013

Bradford, J., McLennan, J., Moore, J., Podgorney, R., Tiwari, S. (2015) Hydraulic and Thermal Stimulation Program at Raft River Idaho, A DOE EGS. *Geothermal Resources Council Transaction*s, 39, 261-268.

Bradford, J.T., Ohren, M., Osborn, W.L., McLennan, J., Moore, J., Podgorney, R. (2014) Thermal Stimulation and Injectivity Testing at Raft River, ID EGS Site. *PROCEEDINGS, Thirty-Ninth Workshop on*

344   *Geothermal Reservoir Engineering* Stanford University, Stanford, California, February 24-26, 2014 SGP-
345   TR-202

346   Chaussard, E., Burgmann, R., Shirzaei, M., Fielding, E.J. & Baker, B., 2014. Predictability of hydraulic head
347   changes and characterization of aquifer-system and fault properties from InSAR-derived ground
348   deformation, *Journal of Geophysical Research: Solid Earth*, 119, 6572-6590.

349   Cihan, A., Birkholzer, J.T. & Bianchi, M., 2015. Optimal well placement and brine extraction for pressure
350   management during CO2 sequestration, *International Journal of Greenhouse Gas Control*, 42, 175-187.

351   Dieterich, J.H., 1994. A constitutive law for the rate of earthquake production and its application to
352   earthquake clustering, *J. Geophys. Res.*, 99, 2601-2618.

353   Dolenc, M. R., Hull, L. C., Mizell, S. A., Russell, B. F., Skiba, P. A., Strawn, J. A., et al. (1981). Raft River
354   geoscience case study. (EGG-2125). Idaho Falls, Idaho: EG&G, Idaho, Inc.

355   Elsworth, D., Fang, Y., Gan, Q., Im, K. J., Ishibashi, T., & Guglielmi, Y. (2016). Induced seismicity in the
356   development of EGS—benefits and drawbacks. In H. Li, J. Li, Q. Zhang, & J. Zhao (Eds.), *Rock Dynamics:*
357   *From Research to Engineering - 2nd International Conference on Rock Dynamics and Applications,*
358   *ROCDYN 2016* (pp. 13-24). CRC Press/Balkema. doi:10.1201/b21378-4

359   Ellsworth, W. (2013) Injection-Induced Earthquakes. *Science*, 341(6142). doi: 10.1126/science.1225942

360   Farr, T. G., Rosen, P. A., Caro, E., Crippen, R., Duren, R., Hensley, S., et al. (2007). The shuttle radar
361   topography mission. *Reviews of Geophysics*, *45*(2), Rg2004. doi: 10.1029/2005rg000183

362   Franceschetti, G., & Lanari, R. (1999). *Synthetic aperture radar processing*. Boca Raton, Florida: CRC
363   Press.

364   Goebel, T.H.W. & Brodsky, E.E. (2018) The spatial footprint of injection wells in a global compilation of
365   induced earthquake sequences. *Science*, 361(6405), 899-904, doi: 10.1126/science.aat5449

366   Goebel, T.H.W., Weingarten, M., Chen, X., Haffener, J. & Brodsky, E.E., 2017. The 2016 Mw5.1 Fairview,
367   Oklahoma earthquakes: Evidence for long-range poroelastic triggering at > 40 km from fluid disposal
368   wells, *Earth and Planetary Science Letters*, 472, 50-61.

369   Goertz-Allman, B.P., Gibbons, S.J., Oye, V., Bauer, R., Will, R. (2017) Characterization of induced
370   seismicity patterns derived from internal structure in event clusters. *Journal of Geophysical Research:*
371   *Solid Earth*, 122(5), 3875-3894, doi: 10.1002/2016JB013731

372   Hooper, A., & Zebker, H. A. (2007). Phase unwrapping in three dimensions with application to InSAR
373   time series. *J. Opt. Soc. Am. A.*, *24*(9).

374   Hoffmann, J., Zebker, H.A., Galloway, D.L. & Amelung, F., 2001. Seasonal subsidence and rebound in Las
375   Vegas Valley, Nevada, observed by synthetic aperture radar interferometry, *Water Resources Research*,
376   37, 1551-1566.

377   Hornbach, M.J., DeShon, H.R., Ellsworth, W.L., Stump, B.W., Hayward, C., Frohlich, C., Oldham, H.R.,
378   Olson, J.E., Magnani, M.B., Brokaw, C., Luetgert, J.H. (2015). Causal factors for seismicity near Azle,
379   Texas. *Nature Communications*, 6, doi: 10.1038/ncomms7728

380　Ito, T. & Zoback, M.D., 2000. Fracture permeability and in situ stress to 7 km depth in the KTB Scientific
381　Drillhole, *Geophysical Research Letters*, 27, 1045-1048.

382　Juanes, R., Jha, B., Hager, B.H., Shaw, J.H., Plesch, A., Astiz, L., Dieterich, J.H. & Frohlich, C., 2016. Were
383　the May 2012 Emilia-Romagna earthquakes induced? A coupled flow-geomechanics modeling
384　assessment, *Geophysical Research Letters*, 43, 6891-6897.

385　King, G.C.P., Stein, R.S. & Lin, J., 1994. Static Stress Changes and The Triggering Of Earthquakes, *Bulletin*
386　*Of The Seismological Society Of America*, 84, 935-953.

387　Kuvshinov, B.N. (2008) Elastic and piezoelectric fields due to polyhedral inclusions. *International Journal*
388　*of Solids and Structures*,45(5), 1352-1384, doi: 10.1016/j.ijsolstr.2007.09.024

389　Kwiatek, G., Saarno, T., Ader, T., Bluemle, F., Bohnhoff, M., Chendorain, M., Dresen, G., Heikkinen, P.,
390　Kukkonen, I., Leary, P., Leonhardt, M., Malin, P., Martinez-Garzon, P., Passmore, K., Pasmore, P.,
391　Valenzuela, S., Wollin, C. (2019) Controlling fluid-induced seismicity during a 6.1-km-deep geothermal
392　stimulation in Finland. *Science Advances*, 5(5), doi: 10.1126/sciadv.aav7224

393　Langenbruch, C. & Zoback, M.D. (2016) How will induced seismicity in Oklahoma respond to decreased
394　saltwater injection rates? *Science Advances*, 2(11), doi: 10.1126/sciadv.1601542

395　Lawrence Berkeley Induced Seismicity EGS. Interactive, Map of Earthquakes at Raft River.
396　http://esd.lbl.gov/research/projects/induced_seismicity/egs/raft_river.html (accessed April, 2021).

397　Liu, F., Fu, P., Mellors, R.J., Plummer, M.A., Ali, S.T., Reinisch, E.C., Liu, Q., Feigl, K.L. (2018) Inferring
398　Geothermal Reservoir Processes at the Raft River Geothermal Field, Idaho, USA, Through Modeling
399　InSAR−Measured Surface Deformation. *Journal of Geophysical Research: Solid Earth*, 123(5), 3645-3666,
400　doi: 10.1029/2017JB015223

401　Lopez-Martinez, C., & Fabregas, X. (2002). Modeling and reduction of SAR interferometric phase noise in
402　the wavelet domain. *Ieee Transactions on Geoscience and Remote Sensing*, *40*(12), 2553-2566. doi:
403　10.1109/TGRS.2002.806997

404　Mignan, A., Landtwing, D., Kastli, P., Mena, B., Wiemer, S. (2015) Induced seismicity risk analysis of the
405　2006 Basel, Switzerland, Enhanced Geothermal System project: Influence of uncertainties on risk
406　mitigation. *Geothermics*, 53, 133-146, doi: 10.1016/j.geothermics.2014.05.007

407　Nash, G.D. & Moore, J.N. (2012) Raft River EGS Project A GIS Centric Review of Geology. *Geothermal*
408　*Resources Council Transaction*s, 36, 951-958.

409　Ramdas, A., Trillos, N.G., Cuturi, M. (2017) On Wasserstein Two-Sample Testing and Related Families of
410　Nonparametric Tests. *Entropy*, 19(2), doi: 10.3390/e19020047

411　Rudnicki, J.W. (1986) Fluid mass sources and point forces in linear elastic diffusive solids. *Mechanics of*
412　*Materials*, 5(4), 383-393

413　Segall, P., Grasso, J.R. & Mossop, A., 1994. Poroelastic stressing and induced seismicity near the Lacq
414　gas-field, southwestern France, *Journal of Geophysical Research: Solid Earth*, 99, 15423-15438.

415　Segall, P. & Fitzgerald, S.D., 1998. A note on induced stress changes in hydrocarbon and geothermal
416　reservoirs, *Tectonophysics*, 289, 117-128.

417   Shapiro, S.A., Huenges, E. & Borm, G., 1997. Estimating the crust permeability from fluid-injection-
418   induced seismic emission at the KTB site, *Geophysical Journal International*, 131, F15-F18.

419   Shirzaei, M. (2013). A Wavelet-Based Multitemporal DInSAR Algorithm for Monitoring Ground Surface
420   Motion. *IEEE Geoscience and Remote Sensing Letters*, *10*(3), 456-460. doi: 10.1109/Lgrs.2012.2208935

421   Shirzaei, M., & Bürgmann, R. (2012). Topography correlated atmospheric delay correction in radar
422   interferometry using wavelet transforms. *Geophysical Research Letters*, *39*(1), L01305. doi:
423   10.1029/2011GL049971

424   Shirzaei, M., & Bürgmann, R. (2013). Time-dependent model of creep on Hayward fault inferred from
425   joint inversion of 18 years InSAR time series and surface creep data. *Journal of Geophysical Research-
426   Solid Earth*, *118*, 1733–1746. doi: 10.1002/jgrb.50149

427   Shirzaei, M., Ellsworth, W.L., Tiampo, K.F., Gonzalez, P.J. & Manga, M., 2016. Surface uplift and time-
428   dependent seismic hazard due to fluid injection in eastern Texas, *Science*, 353, 1416-1419.

429   Shirzaei, M., & Walter, T. R. (2011). Estimating the Effect of Satellite Orbital Error Using Wavelet-Based
430   Robust Regression Applied to InSAR Deformation Data. *Ieee Transactions on Geoscience and Remote
431   Sensing*, *49*(11), 4600-4605. doi: 10.1109/Tgrs.2011.2143419

432   Smith, J. D. (2019). Geomechanical properties of the Groningen reservoir (doctoral thesis). doi:
433   10.17863/CAM.41005

434   Stein, R.S., 1999. The role of stress transfer in earthquake occurrence, *Nature*, 402, 605-609.

435   Stork, A.L., Verdon, J.P., Kendall, J.-M. (2015) The microseismic response at the In Salah Carbon Capture
436   and Storage (CCS) site. *International Journal of Greenhouse Gas Control*, 32, 159-171, doi:
437   10.1016/j.ijggc.2014.11.014

438   Tan, Y., Hu, J., Zhang, H., Chen, Y., Qian, J., Wang, Q., Zha, H., Tang, P., Nie, Z. (2020) Hydraulic Fracturing
439   Induced Seismicity in the Southern Sichuan Basin Due to Fluid Diffusion Inferred From Seismic and
440   Injection Data Analysis. *Geophysical Research Letters*, 47(4). doi: 10.1029/2019GL084885

441   Walter, J.I., Frohlich, C., Borgfeldt, T. (2018) Natural and induced seismicity in the Texas and Oklahoma
442   Panhandles. *Seismological Research Letters*, 89(6), 2437-2446, doi: doi.org/10.1785/0220180105

443   Yuan, Y.L., Xu, T.F., Moore, J., Lei, H.W. & Feng, B., 2020. Coupled Thermo-Hydro-Mechanical Modeling
444   of Hydro-Shearing Stimulation in an Enhanced Geothermal System in the Raft River Geothermal Field,
445   USA, *Rock Mechanics and Rock Engineering*, 53, 5371-5388.

446   Zandt, G, McPherson, L, Schaff, S, & Olsen, S. Seismic baseline and induction studies: Roosevelt Hot
447   Springs, Utah and Raft River, Idaho. *United States*. doi:10.2172/6396329

448   Zhai, G. & Shirzaei, M. (2018). Fluid Injection and Time−Dependent Seismic Hazard in the Barnett Shale,
449   Texas. *Geophysical Research Letters*, 45(10), 4743-4753. doi: 10.1029/2018GL077696

450   Zhai, G., Shirzaei, M., Manga, M., Chen, X. (2019). Pore-pressure diffusion, enhanced by poroelastic
451   stresses, controls induced seismicity in Oklahoma. *Proceedings of the National Academy of Sciences*,
452   116 (33), 16228-16233. doi: 10.1073/pnas.1819225116

453 Zoback, M.D. & Gorelick, S.M., 2012. Earthquake triggering and large-scale geologic storage of carbon

454 dioxide, *Proceedings of the National Academy of Sciences of the United States of America*, 109, 10164-

455 10168. doi: 10.1073/pnas.1202473109

456   ## Tables and Figures

457   **Table 1**: Hydro-and geomechanical properties used for simulation of pore pressures and poroelastic
458   stress changes. The parameters which are calibrated using the surface deformation measurements are
459   shown in bold. The values in parentheses indicate a priori values, and uncertainties at the 95%
460   confidence level are estimated from bootstrap sampling (Supplementary Figure S1).

|	Injection Reservoir	Production Reservoir	Narrows Fault
Fluid density ρ, (kg/m^3)	998	998	
Fluid viscosity, (Pa s)	8.9×10^{-4}	8.9×10^{-4}	
Skempton's coefficient, B	0.75	0.75	
Permeability, k (m^2)	**$5.9 \pm 1.5 \times 10^{-13}$ (4.7×10^{-13})**	**$5 \pm 1.3 \times 10^{-13}$ (4×10^{-13})**	
Porosity	0.15	0.15	
Compressibility, C$_m$ (Pa^{-1})	**$6.1 \pm 0.3 \times 10^{-9}$ (5.1×10^{-9})**	**$2.5 \pm 0.4 \times 10^{-10}$ (2.04×10^{-9})**	
Shear modulus, μ (GPa)	0.833	2.08	
Thickness, (m)	300	100	
Biot coefficient, α	0.31	0.31	
Poisson's ratio, ν	0.2	0.2	
Flow anisotropy factor, ξ	1.4	1.4	
Flow anisotropy angle, φ	20° (slow diffusion N70^{o}E)	20° (slow diffusion N70^{o}E)	
Friction angle, (^{o})			31
Strike, (^{o})			N60^{o}E
Dip, (^{o})			76
Sense			Sinistral

461

Figure 1: Summary showing a) the geodetically measured surface displacement rate during 2007-2011, location of injection and production wells, and detected earthquakes; b) southeast-northwest depth cross section of simplified site geology, showing well and earthquake locations; c) modelled surface displacement rate; d) time evolution of seismicity rate and measured and modelled surface displacements at point "A". DOE experimental well RRG-9, which is injecting into the production reservoir, is shown in the yellow square. Vertical displacement referenced as positive upwards, depths referenced to sea level. EQ = Earthquake.
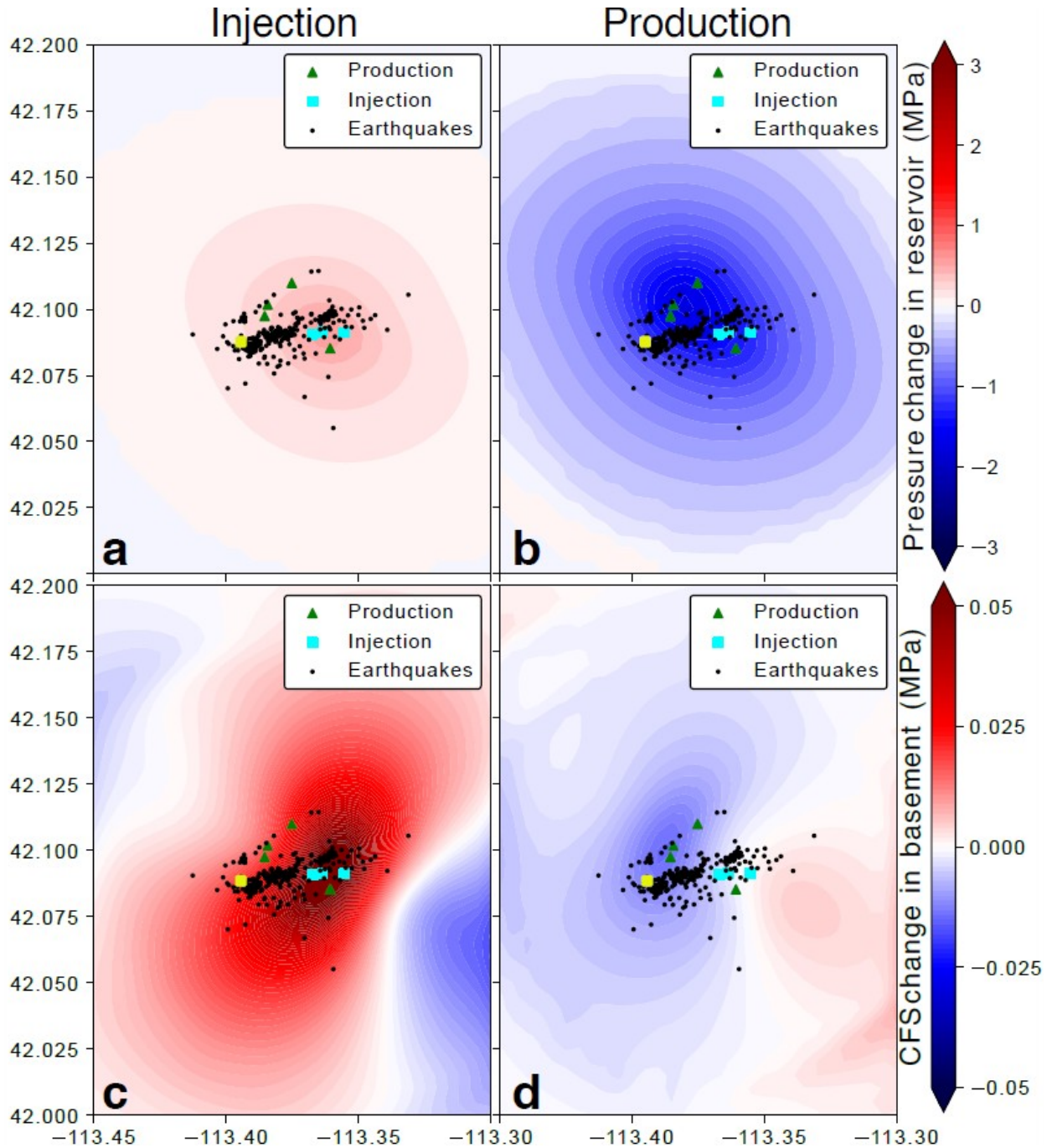
Figure 2: Spatial maps of pressure change in the reservoirs in April 2014 corresponding to a) injection, b) production; and Coulomb failure stress (CFS) changes in the basement attributed to c) injection and d) production, calculated on a steeply dipping left-lateral N60E fault.
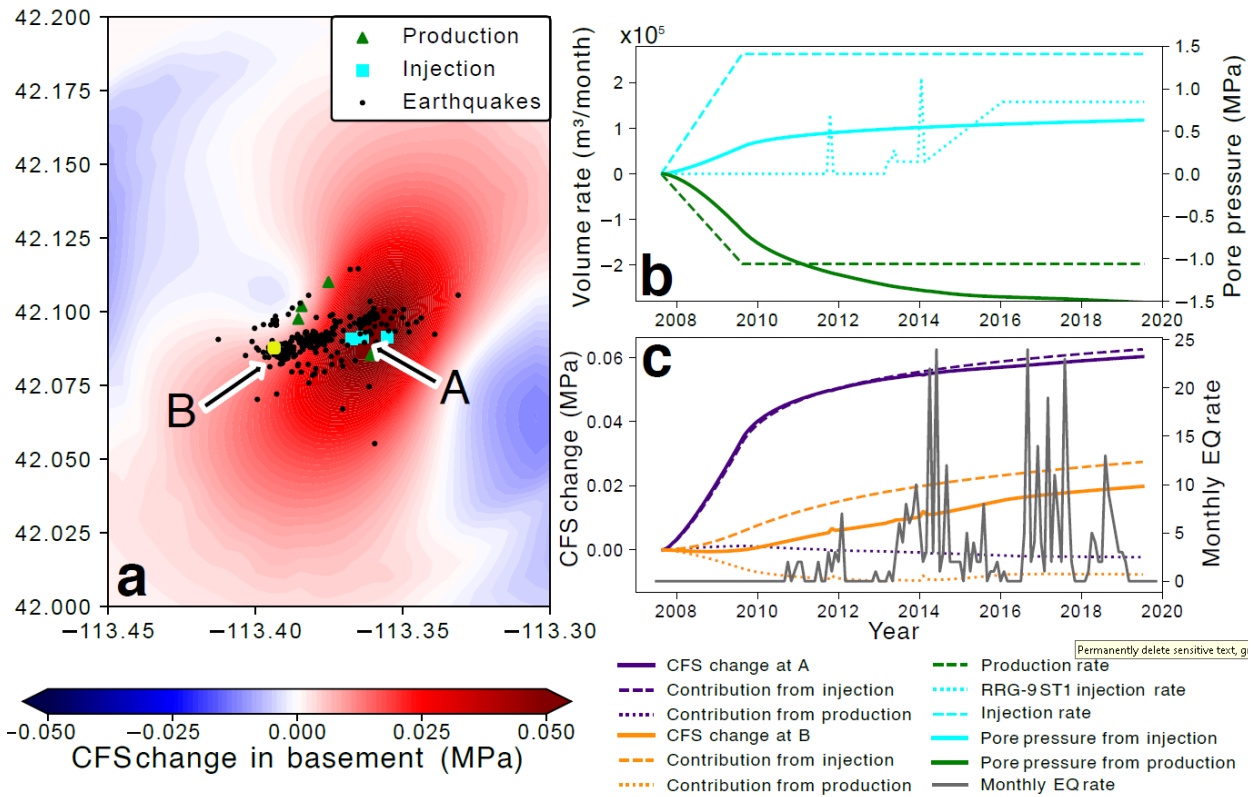
Figure 3: Modelled Coulomb failure stress (CFS) changes in the basement due to the combined effects of injection and production. a) shows the spatial distribution of CFS in the basement in April 2014, b) shows the imposed volume rates, c) shows the modelled CFS change at points "A" and "B" (Figure 1b) in the basement over time, alongside the measured seismicity rate.
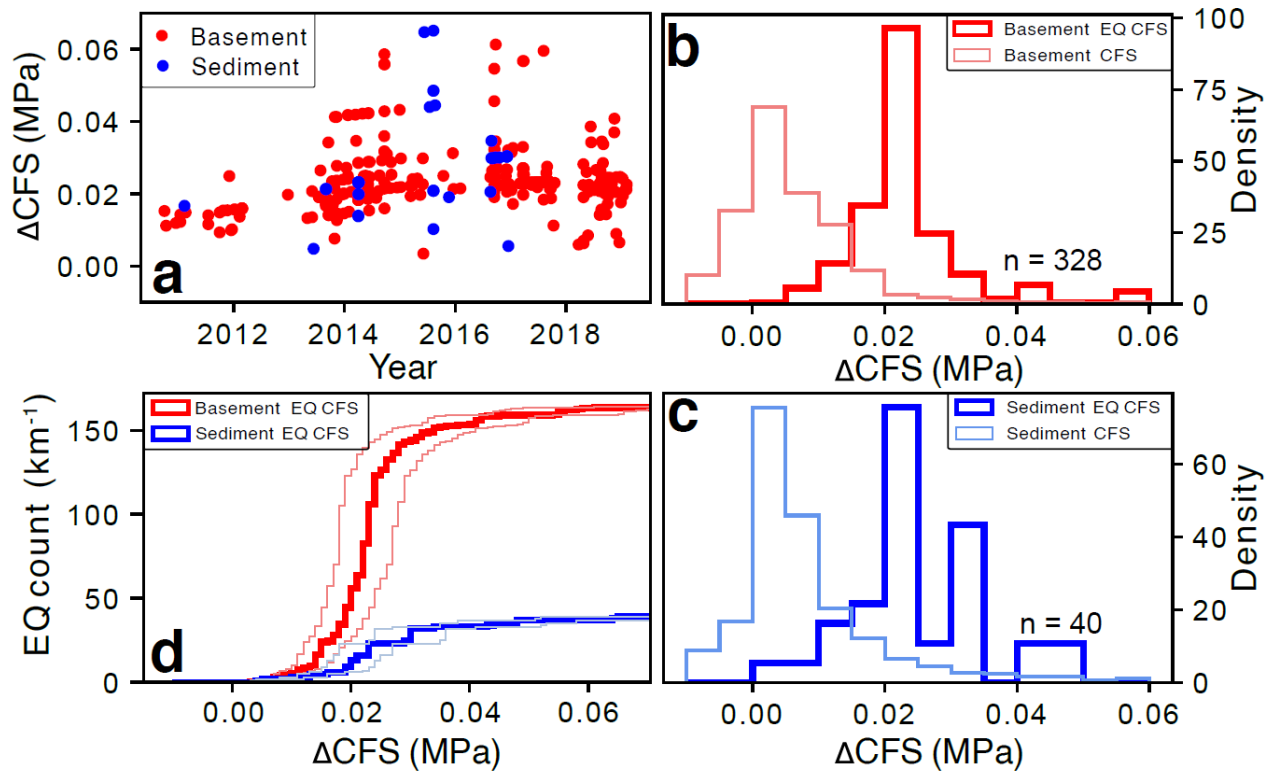
479

480 **Figure 4**: Coulomb failure stress (CFS) at time and location of detected earthquakes, a) shown over time
481 for events detected in the basement and the overlying sedimentary cover. b) and c) show the
482 histograms of the CFS at earthquake nucleation compared to the overall distribution of CFS in the
483 basement and sedimentary cover formation respectively. d) Cumulative histogram of CFS at earthquake
484 nucleation for the basement and the sedimentary cover, normalized by the thickness of the activated
485 rock (1km for sediment, 2km for basement). Light coloured lines indicate 95% confidence intervals
486 estimated according to bootstrap sampling (Supplementary Figure S1). EQ = Earthquake.

487

488 Supplement 1 - Spatio-temporal evolution of surface deformation

489 Following on previous studies (Ali et al., 2018; Liu et al.), we use Interferometric Synthetic Aperture

490 Radar (InSAR) to measure the time evolution of surface deformation associated with the geothermal

491 operations at the Raft River site. To this end, we use a wavelet-based multitemporal InSAR algorithm,

492 so-called WabInSAR (Shirzaei, 2013; Shirzaei & Bürgmann, 2013), applied to a time series of L-band SAR

493 images. The data set is comprised of 17 Level 1.0 Single-Look Complex (SLC) images acquired by ALOS

494 PALSAR in the ascending path #204 and frame #830, spanning 6/13/2007 to 2/6/2011. To reduce the

495 effect of speckle noise, SLCs are multilooked with a factor of 10 and 16 along the range and azimuth,

496 respectively, generating pixels with size of 47m × 50m. All the SLCs are then accurately coregistered to a

497 single reference image, which is chosen in a way that minimizes the total spatiotemporal baseline. We

498 then form 90 interferograms between pair of SLC images whose acquisition dates is less than 1500 days

499 apart and their perpendicular baseline (a parameter related to the orbital position of the satellite during

500 the two acquisitions) is shorter than 2 km. The interferograms are then flattened using satellite

501 ephemeris data and a Digital Elevation Model (DEM) with 30m resolution provided by the Shuttle Radar

502 Topography Mission (SRTM) (Farr et al., 2007) to remove the effects of a flat earth and surface

503 topography (Franceschetti & Lanari, 1999). The elite (i.e., less noisy) pixels are next identified using a

504 statistical test, which investigates the time series of complex interferometric phase noise in the wavelet

505 domain (Lopez-Martinez & Fabregas, 2002; Shirzaei, 2013). Next, the absolute estimates of the phase

506 change associated with the identified elite pixels is obtained by applying an iterative three-dimensional

507 phase unwrapping algorithm (Hooper & Zebker, 2007).

508 A set of wavelet-based filters are used to remove the nuisance signal associated with various sources of

509 error in the unwrapped interferograms. The spatially correlated nuisance terms are mainly caused by

510 the atmospheric delay and the orbital and satellite clock errors. To remove these errors, each

511   unwrapped interferogram is decomposed into its high-pass and low-pass sub-bands using a two-

512   dimensional multiresolution wavelet transformation. The effect of residual orbital errors is removed by

513   fitting a 2nd order polynomial to the average component (i.e., the high-pass sub-band) through a robust

514   regression method (Shirzaei & Walter, 2011). On the other hand, the details coefficients (i.e., the low-

515   pass sub-bands) are down-weighted according to their correlation with the corresponding details

516   coefficients associated with the DEM of the study area to correct the interferogram for the phase

517   contributions from the topography-correlated component of atmospheric delay (Shirzaei & Bürgmann,

518   2012). Moreover, the detail coefficients are further refined using a low-pass filter generated based on

519   the Legendre polynomial wavelets to reduce the effect of residual DEM error, which appears as a high-

520   spatial-frequency noise (Shirzaei, 2013).

521   The corrected unwrapped interferograms are then inverted using an iterative re-weighted least squares

522   method (O'leary, 1990), where the weight of observation in each iteration changes based on the

523   residuals from the previous iteration (Shirzaei, 2013), to obtain the deformation time series. Surface

524   deformation rate at the location of elite pixels is then estimated as the slope of best-fitting line to the

525   associated time series. Assuming all the deformation are vertical, the line-of-sight (LOS) observation is

526   finally converted to the up-down direction using the LOS unit vector, which is a function of incidence

527   angle at the location of elite pixels.

Supplement 2 – Full Poroelastic Solutions

528

529   Here, ΔP is the pressure change in the grid cell in the reservoir, vertices with index *i* referring to the

530   vertices of the grid cell, $R_{\pm} = \left(\overline{x}^2 + \overline{y}^2 + \zeta_{\pm}^2\right)^{\frac{1}{2}}$, $\zeta_{\pm} = z_i \pm z_{eval}$, $\overline{x}_i = x_i - x_{eval}$ etc., and x_{eval} denotes the

531   location where the stress or displacement is evaluated.

532    $\sigma_{xx}(x, t) = \Delta P \dfrac{\alpha C_m \mu}{2\pi} \displaystyle\sum_{vertices} (-1)^{i-1} ¿¿$

533    $\sigma_{yy}(x, t) = \Delta P \dfrac{\alpha C_m \mu}{2\pi} \displaystyle\sum_{vertices} (-1)^{i-1} ¿¿$

534 $\quad \sigma_{zz}(x,t) = \Delta P \dfrac{\alpha\, C_m \mu}{2\pi} \displaystyle\sum_{vertices} (-1)^{i-1}\, \textdbend\, \textdbend$

535 $\quad \sigma_{xy}(x,t) = -\Delta P \dfrac{\alpha\, C_m \mu}{2\pi} \displaystyle\sum_{vertices} (-1)^{i-1}\, \textdbend\, \textdbend$

536 $\quad \sigma_{xz}(x,t) = \Delta P \dfrac{\alpha\, C_m \mu}{2\pi} \displaystyle\sum_{vertices} (-1)^{i-1}\, \textdbend\, \textdbend$

537 $\quad \sigma_{yz}(x,t) = \Delta P \dfrac{\alpha\, C_m \mu}{2\pi} \displaystyle\sum_{vertices} (-1)^{i-1}\, \textdbend\, \textdbend$

538 $\quad U_x(x,t) = \Delta P \dfrac{\alpha\, C_m}{4\pi} \displaystyle\sum_{vertices} (-1)^{i-1}\, \textdbend$

539 $\quad U_y(x,t) = \Delta P \dfrac{\alpha\, C_m}{4\pi} \displaystyle\sum_{vertices} (-1)^{i-1}\, \textdbend$

540 $\quad U_z(x,t) = -\Delta P \dfrac{\alpha\, C_m}{4\pi} \displaystyle\sum_{vertices} (-1)^{i-1}\, \textdbend$

541 $\quad f(x,y,Z,R) = Z atan\left(\dfrac{xy}{ZR}\right) - x ln(R+y) - y ln(R+x)$

542

543   Supplement 3 – Supplemental Figures and Tables

544
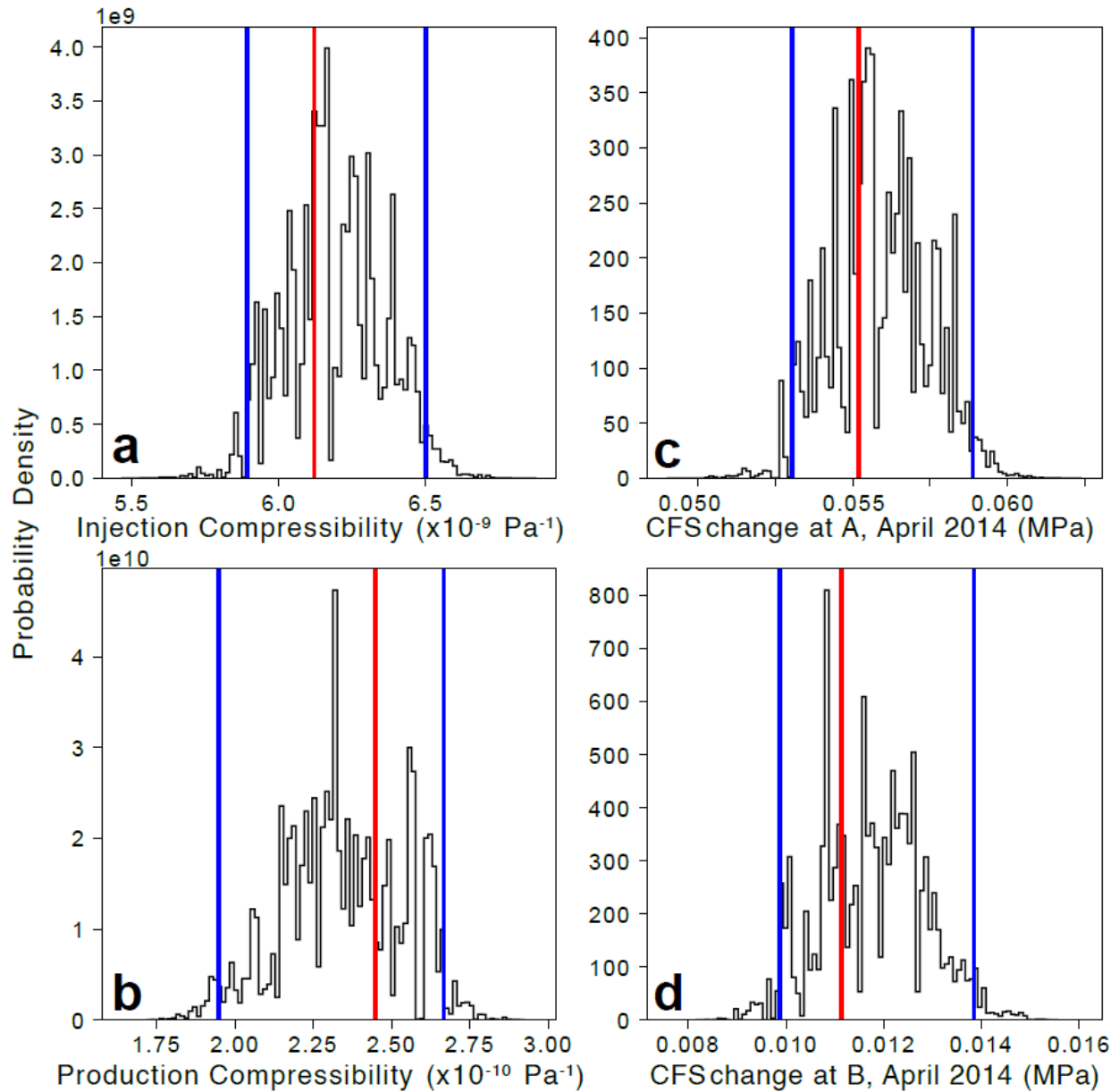
Figure S1: Results of 100,000 bootstrap samples each of size 10,000 to quantify model uncertainty. a) histogram of best-fit injection reservoir compressibility, b) histogram of best-fit production reservoir compressibility, c) histogram of best-fit Coulomb failure stress (CFS) change values at point "A" in Figure 1a, d) histogram of CFS change at point "B" Figure 3a. Red lines indicate overall best fit model, based on 1,000,000 generated samples, and blue lines indicate 2.5th and 97.5th percentiles denoting the 95% confidence range.
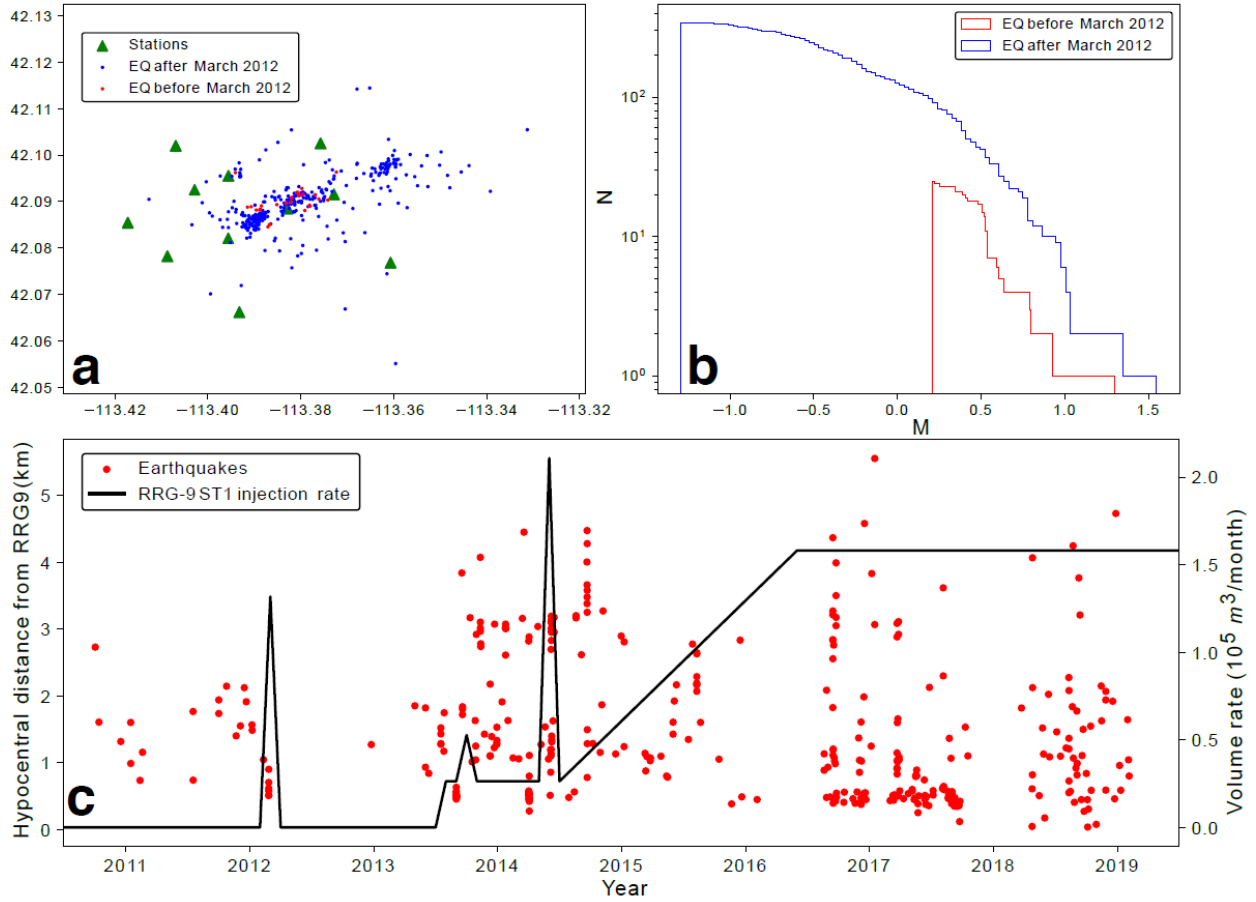
Figure S2: Summary plots showing a) location of seismicity before and after the first hydraulic stimulation in March 2012 alongside station locations, b) Frequency-Magnitude distribution of events, c) timing and distance of earthquakes relative to the RRG-9 wellhead.
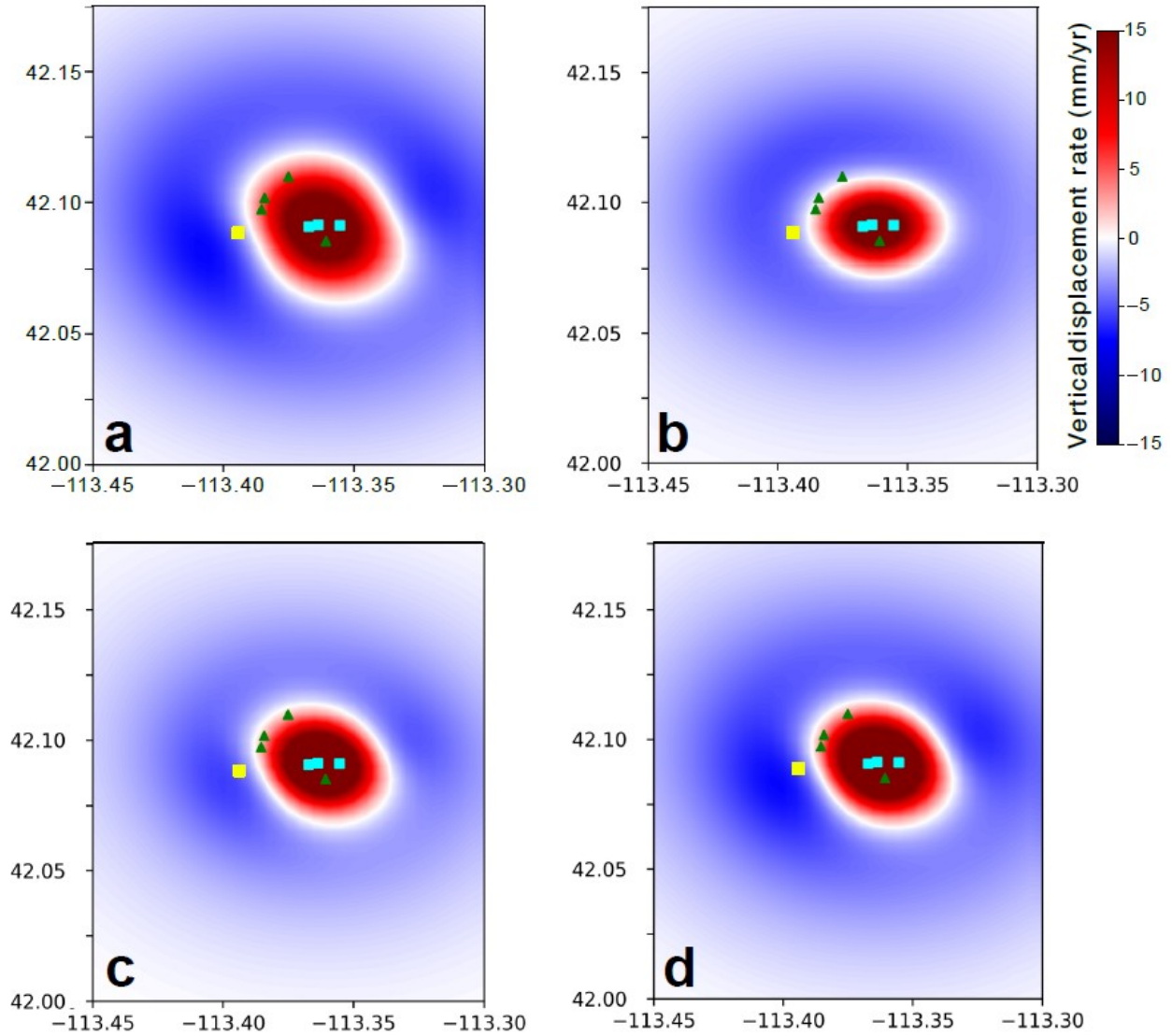
Figure S3: Comparison of modelled surface displacement from a) optimal model with anisotropy, b) isotropic model, c) model with injection reservoir permeability = 4.7 x 10^{-13} m^2, production reservoir permeability = 4 x 10^{-13} m^2, d) model with injection reservoir permeability = 7.1 x 10^{-13} m^2, production reservoir permeability = 6 x 10^{-13} m^2.
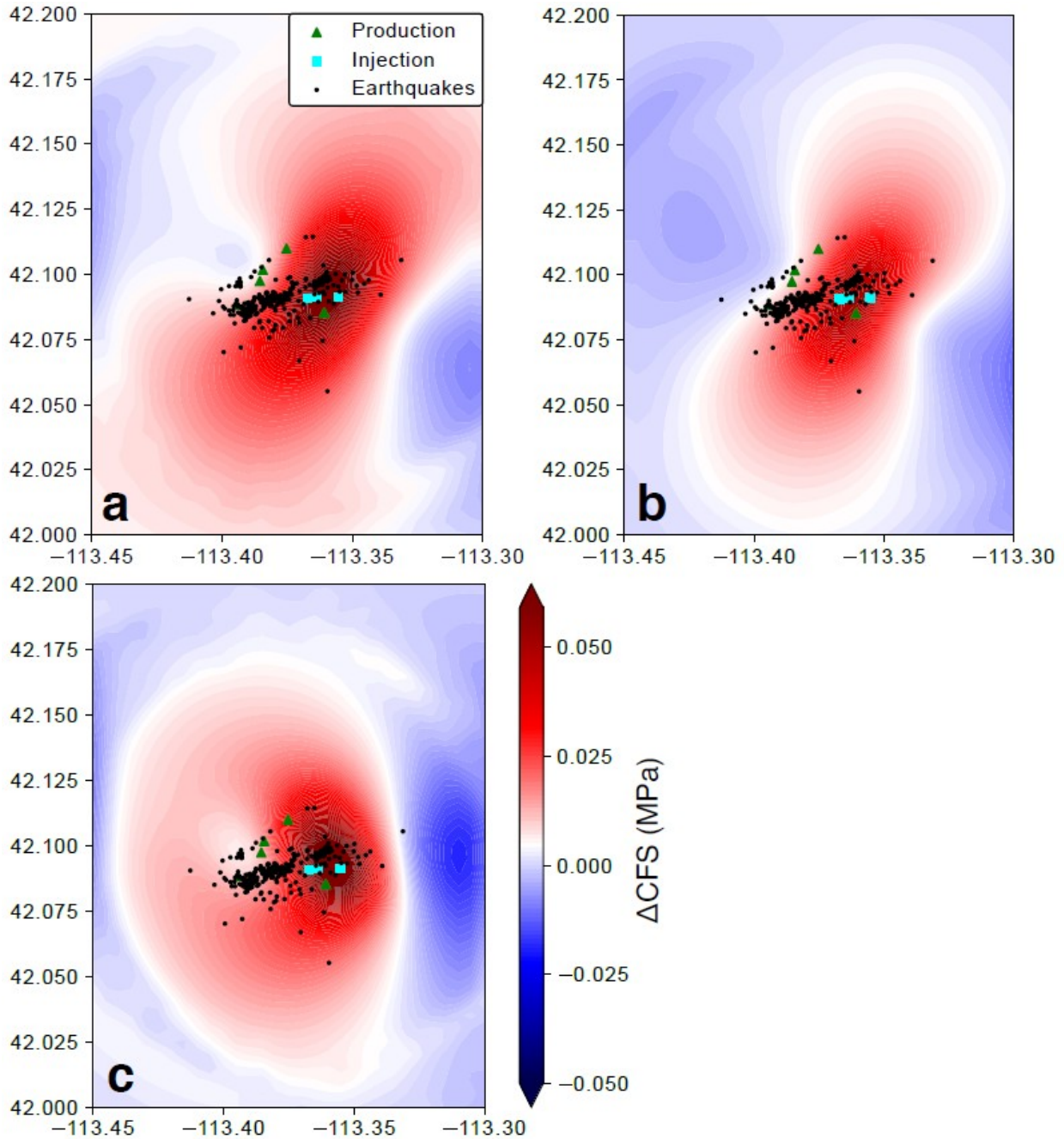
Figure S4: Comparison of effect of assumed fault plane (left-lateral N60E), a) shows model where CFS is calculated along the left-lateral N60E Narrows fault zone, b) model where CFS is calculated along left-lateral N-S striking faults, c) model where CFS is calculated along a normal-faulting N-S fault.